J. Appl. Comput. Mech., 12(4) (2026) 1490-1506
DOI: 10.22055/jacm.2025.48846.5544

ISSN: 2383-4536
jacm.scu.ac.ir

Shahid Chamran University of Ahvaz

Journal of Applied and Computational Mechanics

Research Paper

Comparative Optimization of Vibrational Properties in Tensegrity Structures via Spectral Element Method

Juan C. Guacheta-Alba[1], Luciano Santos Constantin Raptopoulos[2,3], Max Suell Dutra[1]

[1] Robotics Laboratory, Mechanical Engineering Department, Universidade Federal do Rio de Janeiro, Rio de Janeiro, Brazil, Email: juan.camilo@mecanica.coppe.ufrj.br (J.C.G.A.); max@mecanica.coppe.ufrj.br (M.S.D.)

[2] Postdoctoral Program, Robotics Laboratory, Mechanical Engineering Department, Universidade Federal do Rio de Janeiro, Rio de Janeiro, Brazil

[3] Federal Center of Technological Education Celso Suckow da Fonseca, CEFET-RJ, Campus de Nova Iguaçu, RJ, Brazil, Email: luciano.raptopoulos@cefet-rj.br

Received October 21 2025; Revised December 12 2025; Accepted for publication December 18 2025.
✉ Corresponding author: J.C. Guacheta-Alba (juan.camilo@mecanica.coppe.ufrj.br)
© 2026 Published by Shahid Chamran University of Ahvaz

Abstract. This paper presents a systematic framework for the vibration-based optimization of tensegrity structures, integrating the Spectral Element Method (SEM) with a Particle Swarm Optimization (PSO) strategy to explore metric-specific performance across representative tensegrity configurations. The SEM formulation provides exact frequency-dependent stiffness without spatial discretization, ensuring high numerical precision in the evaluation of natural frequencies and frequency response functions (FRFs). Five dynamic-oriented metrics—Dynamic Efficiency (DE), Minimum Modal Separation (MMS), Modal Density Ratio (MDR), Prestress Robustness (PR), and Critical FRF Magnitude (CFM)—are individually optimized for four representative tensegrity topologies, allowing a comparative assessment of convergence behavior, sensitivity, and robustness. Results reveal clear trends: stiffness-related metrics (DE, CFM) exhibit stable convergence and low dispersion, producing geometrically balanced tensegrities with uniform prestress distributions. In contrast, modal and robustness-oriented objectives (MMS, MDR, PR) are more sensitive to configuration and prestress variations, yielding asymmetric arrangements and higher variability across optimization runs. Complex topologies (C and D) show amplified convergence dispersion, confirming that structural complexity increases the difficulty of identifying global optima under dynamic criteria. The findings demonstrate that PSO effectively captures distinct vibrational optima and that the interplay between topology, pretension, and modal coupling governs the dynamic performance of tensegrity systems. The proposed approach provides a unified framework for quantifying vibrational trade-offs and metric robustness, establishing a foundation for the vibration-tailored design of tensegrity structures and their dynamic optimization.

Keywords: Tensegrity, Spectral element method, Vibration metrics, Particle swarm optimization.

1. Introduction

Tensegrity structures, composed of axially prestressed tension members and isolated compression elements, have attracted growing interest due to their unique combination of flexibility, lightweight efficiency, and mechanical resilience, making them suitable for a wide range of advanced engineering applications. For instance, Mei et al. [1] and Guacheta-Alba et al. [2] demonstrated their use in soft robotics and vibration-driven locomotion devices for disaster rescue, while Goyal and Skelton [3] explored their potential in deployable space structures such as antennas and solar wings. In civil engineering, Liu et al. [4] investigated modular pedestrian bridges that exploit tensegrity's adaptive load-bearing capabilities; their distinctive architecture allows modular assembly, rapid deployment, and remarkable stability under dynamic loads [5]. Representative tensegrity unit cells are depicted in Fig. 1, highlighting the variety of geometries considered in tensegrity design. The same properties that make tensegrity systems advantageous also lead to highly coupled dynamics, low-order vibration modes, and infinitesimal kinematic mechanisms, complicating the prediction of their vibrational behavior [2, 6, 7]. Understanding these characteristics is essential for achieving desired motion or stability in mobile tensegrity robots [1, 2], optimizing prestress distributions, ensuring structural robustness, and enabling structural health monitoring [5, 8]. Despite advances in linearized and nonlinear dynamic modeling [6, 7] and experimental techniques including full-field mode identification using 3D scanning laser vibrometry [8], challenges remain in capturing full-field dynamics under uncertain loading or when optimizing vibrational response [9].

While these structural characteristics enable diverse applications, they also pose significant challenges in accurately modeling dynamic behavior. Conventional numerical approaches, such as the Finite Element Method (FEM), often struggle to represent the complex prestress-dependent behavior of tensegrity systems [6, 10-12]. As reported by Liu et al. [6] and Gan [13], the presence of low-order rigid-body modes in free-free tensegrity systems, combined with the slenderness and flexibility of the cables, frequently leads to singular stiffness matrices and numerical instabilities in standard FEM formulations. Moreover, geometric nonlinearity

Published online: December 28 2025

induced by prestressing plays a critical role in predicting natural frequencies accurately, yet it is often neglected or inadequately modeled in commercial FEM solvers, particularly when using simplified hinge connections or linearized beam elements [6,14,15]. High-order vibrational modes and complex interactions between struts and cables further increase computational cost and reduce efficiency, making large-scale or high-fidelity analyses computationally prohibitive [14-16]. Additional difficulties arise from sliding or slackening of cables, as these introduce non-smooth dynamics and discontinuities that conventional FEM cannot efficiently handle without specialized formulations, such as co-rotational or complementarity approaches [15]. These challenges are even more pronounced in clustered or hybrid tensegrity configurations, where rigid–flexible coupling and multibody interactions complicate accurate frequency prediction and modal analysis [13, 14]. To address these issues, alternative modeling techniques capable of providing frequency-dependent solutions that inherently include prestress effects and capture both low- and high-frequency dynamics have been proposed [13, 17]. Among these, the Spectral Element Method (SEM) has emerged as a particularly promising approach. As highlighted by Gan [13] and Akhtar and Sunny [17], SEM provides an analytical treatment of axial and transverse member vibrations, eliminates singularity problems, and directly incorporates prestress effects—making it especially suitable for vibration-based analysis and design of tensegrity systems.

These limitations motivate the search for alternative numerical approaches capable of accurately capturing the coupled dynamics and prestress effects inherent in tensegrity structures. Among these, the Spectral Element Method (SEM) has emerged as a particularly promising solution. This high-fidelity method enables modeling the dynamic behavior of axially prestressed members, allowing the exact computation of natural frequencies and mode shapes—something often unattainable with conventional finite element solvers due to rigid-body motions and self-equilibrated prestress states [18, 19]. Gan and Kiryu [18] first demonstrated that SEM can capture the coupled axial and transverse vibrations of tensegrity members with remarkable accuracy, while later studies by Gan [19] extended its application to a broader class of prestressed structures. By employing frequency-dependent stiffness matrices derived from member vibrations, SEM inherently incorporates prestress effects and eliminates the spatial discretization errors typical of FEM, ensuring high numerical precision even for slender cables and lightweight struts [18, 20].

This capability is particularly advantageous for analyzing complex tensegrity topologies characterized by coupled vibration modes, where conventional FEM often struggles to resolve low-order rigid-body and infinitesimal kinematic mechanisms [21,22]. Wang et al. [22] further showed that SEM facilitates efficient optimization by integrating geometric stiffness and prestress directly into the dynamic analysis framework. SEM's analytical treatment of member dynamics also enables robust and computationally efficient frequency tracking through algorithms such as the Wittrick–Williams method [18, 20], ensuring accurate modal identification in both small- and large-scale assemblies. Beyond engineering-scale systems, Nouchi et al. [22] applied SEM to biological analogues such as cytoskeletal tensegrity networks, demonstrating its versatility in capturing multiscale vibrational behavior. Related studies on phononic and tensegrity-inspired metamaterials have shown that SEM can effectively predict bandgap formation and energy localization phenomena [23-26]. Furthermore, SEM proves advantageous for optimization tasks, as it precisely evaluates frequency-dependent responses while minimizing computational cost, eliminating the need for excessive mesh refinement [22]. Finally, as Vangelatos et al. [23] demonstrated, SEM's robustness extends to multistable tensegrity lattices, where exact dynamic solutions are essential for designing structures with tunable or localized vibrational properties.

Leveraging SEM's precise modeling capabilities, researchers have integrated it with optimization strategies to both predict and enhance the dynamic performance of tensegrity systems. Previous studies on tensegrity optimization have often focused on static criteria such as material efficiency, stiffness maximization, or weight minimization, sometimes overlooking the complex interactions between topology, prestress, and dynamic behavior [22, 27, 28]. Jankowski et al. [27] provided a broad review of topology, size, and shape optimization in civil structures, while Wang et al. [20] extended these concepts to tensegrity and prestressed cable–strut systems, emphasizing the role of geometric stiffness in the optimization process. Classical force-based formulations and early topology optimization schemes, however, frequently struggle to handle kinematically indeterminate systems or account for the geometric stiffness introduced by self-stress, potentially excluding innovative high-performance configurations [22, 29].

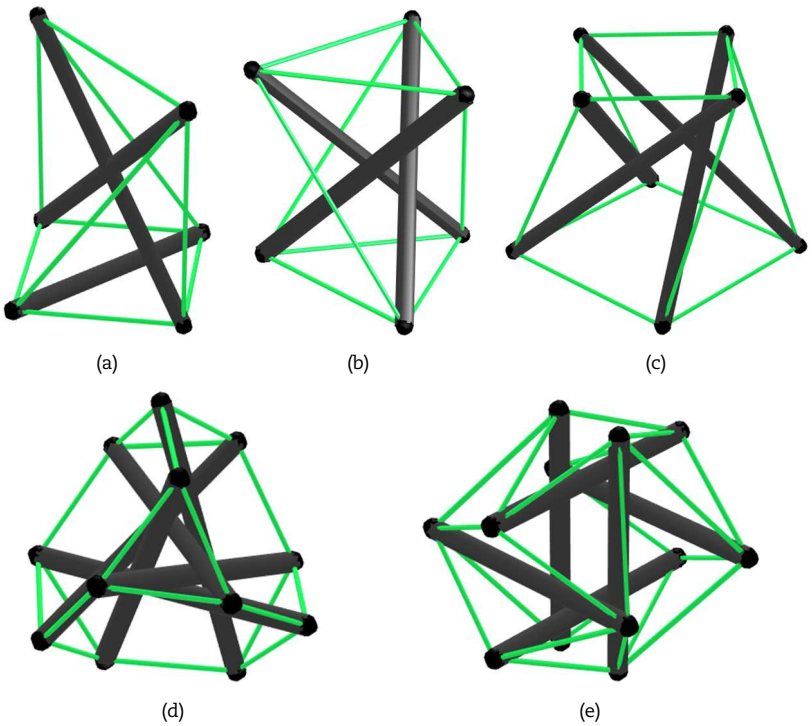

Fig. 1. Representative Tensegrity Unit Cells (from left to right: (a) X-Module, (b) 3-Strut Simplex, (c) 4-Strut Simplex, (d) Truncated Tetrahedron, (e) Expanded Octahedron).

Recent developments have employed metaheuristic optimization methods such as particle swarm optimization (PSO), genetic algorithms, and artificial fish swarm algorithms to improve both dynamic and control performance [27, 29, 30]. For example, Feng et al. [30] implemented a fast model predictive control strategy for active vibration suppression, while Xiong et al. [29] used a multi-population genetic algorithm to optimize actuator placement in cable–strut structures. These vibration-oriented approaches rely on performance indicators including dynamic efficiency, modal separation, eigenfrequency maximization, and prestress robustness, providing insight into energy distribution among modes and system resilience under variations in prestress or boundary conditions [29, 30-32]. Nevertheless, many existing studies still depend on simplified FEM formulations or reduced-order approximations, which can produce inaccuracies in natural frequency and mode shape estimation, particularly in highly prestressed or multi-layer tensegrity lattices [30-32]. Emerging machine-learning and neural-operator approaches, such as physics-informed machine learning and neural operators, offer mesh-free formulations, can naturally incorporate uncertainties, and enable fast surrogate evaluations once trained. However, these methods typically require large training datasets and do not yet provide explicit control of prestress-dependent stability, which are central to tensegrity behavior [33, 34]. To overcome these limitations, integrating SEM with metaheuristic optimization algorithms such as PSO enables precise evaluation of frequency-dependent stiffness matrices and dynamic sensitivities, thereby improving both accuracy and convergence in topology and prestress optimization [20, 27, 35, 36]. This integrated strategy supports the design of large-scale and deployable tensegrity systems [22, 32] and opens the way to advanced applications, including multistable lattices [37], bio-inspired and cellular tensegrity analogues [36, 38], and adaptive structures with tailored dynamic properties [31, 37].

This article introduces a unified spectral-based framework for the dynamic analysis and optimization of tensegrity structures. The approach integrates the Spectral Element Method (SEM) formulation for prestressed members—capable of capturing exact frequency-dependent stiffness—with a Particle Swarm Optimization (PSO) layer tailored to handle complex, multimodal design spaces. This combination enables accurate evaluation and enhancement of dynamic properties such as modal distribution, frequency separation, and prestress robustness, while maintaining high computational efficiency compared to conventional FEM. By explicitly accounting for geometric stiffness, prestress effects, and mechanism-compatible subspaces, the methodology bridges the gap between high-fidelity spectral modeling and optimization, offering a systematic route to design dynamically adaptive tensegrity configurations. The remainder of this paper is structured as follows: Section 2 presents the spectral formulation for prestressed elements and its extension to tensegrity assemblies; Section 3 introduces the dynamic objective functions and optimization methodology; Section 4 describes the simulation setup and optimization cases; Section 5 presents and discusses the numerical results; and Section 6 concludes with the main findings and perspectives for future research on spectral-based optimization of tensegrity systems.

2. Spectral Element Model (SEM) of Tensegrity Structures

The free vibrations of axially prestressed members are analyzed using the Spectral Element Method (SEM), a high-fidelity approach that incorporates frequency dependence directly into the shape functions (dynamic shape functions) and yields an exact dynamic stiffness matrix for each element. Unlike the classical Finite Element Method (FEM), which relies on polynomial interpolation and requires a fine mesh to accurately capture high-frequency responses, SEM expresses the solution in terms of the exact wave modes of each member. This allows it to represent short-wavelength phenomena with a minimal number of degrees of freedom, significantly improving computational efficiency without compromising accuracy [18].

Figure 2 illustrates the representation of an axially prestressed member using both SEM and FEM. Figure 2(a) depicts a single spectral element under axial prestress, showing nodal displacements, internal forces, and the decomposition of the axial wave field into incident and reflected components. Figure 2(b) highlights the fundamental distinction between FEM and SEM: while FEM discretizes the member into multiple low-order elements using polynomial interpolation, SEM employs a single high-order element that provides a continuous and highly accurate approximation of the axial field. This comparison underscores the precision and efficiency of SEM in capturing both dynamic and static behavior of prestressed members, which is essential for high-fidelity modeling of tensegrity structures [18].

This property makes SEM particularly suitable for tensegrity structures, where axially prestressed members dominate the transverse dynamics and the system exhibits rigid-body modes and mechanisms that complicate the use of conventional eigenvalue solvers. The Spectral Element Method (SEM) provides a high-fidelity approach for modeling axially prestressed members, which is particularly suitable for tensegrity structures. In these systems, the axial prestress dominates the transverse dynamics, and the presence of rigid-body modes and internal mechanisms makes conventional finite element eigenvalue solvers less efficient or even inaccurate. For a prestressed prismatic member, assuming small transverse vibrations $w(x,t)$, linear mass density ρA, and constant axial force N (positive in tension), the governing equation of motion in the time domain is expressed as Eq. (1), with nodal boundary conditions $w(0,t) = u_1(t)$ and $w(L,t) = u_2(t)$:

$$\rho A \frac{\partial^2 w(x,t)}{\partial t^2} - N \frac{\partial^2 w(x,t)}{\partial x^2} = 0, \quad 0 < x < L \tag{1}$$

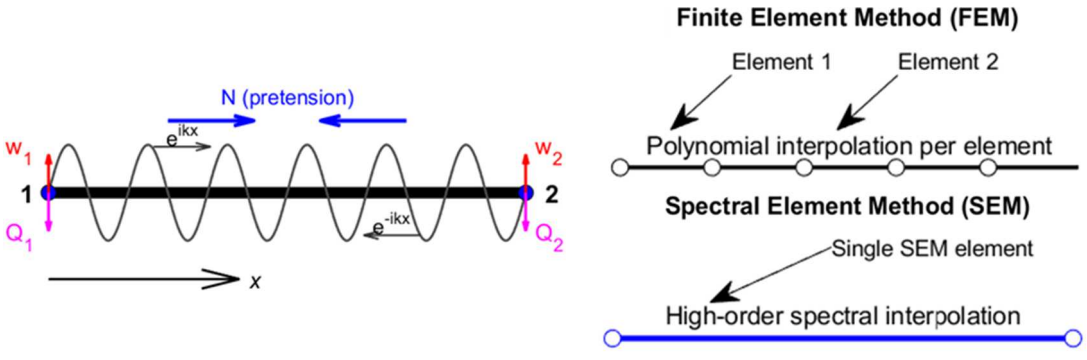

(a) (b)

Fig. 2. Comparison of Axial Member Representations: (a) Prestressed spectral element; (b) FEM vs. SEM discretization.

Assuming a harmonic time dependence $w(x,t) = W(x)e^{i\omega t}$, the weak form of Eq. (1) is obtained by multiplying by an admissible test function $v(x)$ and integrating by parts, yielding the Eq. (2). The corresponding strong form reduces to Eq. (3), with general solution in Eq. (4). Here, the wavenumber k may be real or imaginary depending on the sign of the axial force N, indicating oscillatory or exponentially decaying components, respectively. SEM naturally accommodates both cases by expressing the elemental dynamic shape functions in terms of these exponential functions, without the need for polynomial interpolation [18]:

$$\int_0^L \rho A W(x) v(x) dx + \int_0^L N W(x)' v(x)' dx = 0 \tag{2}$$

$$N \frac{d^2 W(x)}{dx^2} + \omega^2 \rho A W(x) = 0 \tag{3}$$

$$W(x) = Ae^{ikx} + Be^{-ikx}, \quad k^2 = -\frac{\omega^2 \rho A}{N} \tag{4}$$

In a tensegrity structure, each member is prestressed by an internal axial force. Let q_e denote the prestress coefficient of element e, which scales the axial force according to its length L_e and material stiffness. The axial force in element e is then Eq. (5), where E and A are the Young's modulus and cross-sectional area, respectively. This formulation connects the theoretical SEM model to the computational implementation, where q_e is specified for each member:

$$N_e = q_e, \;\; L_e, \;\; E_e, \;\; A_e \tag{5}$$

From the dynamic shape functions, the elemental spectral stiffness matrix $S^{(e)}(\omega)$ is constructed in closed form, relating nodal forces to displacements at a given frequency in Eq. (6), where $H^{(e)}(\omega)$ contains the dynamic shape functions and $D^{(e)}(\omega)$ represents the material and geometric properties of the element:

$$S^{(e)}(\omega) = H^{(e)}(\omega)^{\mathrm{T}} D^{(e)}(\omega) H^{(e)}(\omega) \tag{6}$$

Each elemental matrix $S^{(e)}(\omega)$ is defined in the local coordinate system aligned with the element axis. To assemble the global spectral matrix, a coordinate transformation is applied via the matrix $T^{(e)}$, such that in Eq. (7), where $T^{(e)}$ contains the direction cosines of the local axes (x_i, y_i, z_i) with respect to the global axes. This procedure ensures that the dynamic response of each 3D member is correctly represented in the global structure, preserving both orientation and prestress effects:

$$S^{(e)}_{\text{global}}(\omega) = {T^{(e)}}^{\mathrm{T}} S^{(e)}(\omega) T^{(e)} \tag{7}$$

Each elemental matrix is then transformed to global coordinates via a transformation matrix $T^{(e)}$ and assembled according to the element connectivity $A^{(e)}$ in Eq. (8). The global frequency-dependent matrix $S_s(\omega)$ contains the exact implicit dynamic response of the structure at each frequency. The free-vibration natural frequencies are obtained by seeking ω such that non-trivial displacements $u \neq 0$ satisfy the homogeneous system in Eq. (9):

$$S_s(\omega) = \sum\nolimits_{e=1}^{n_e} {A^{(e)}}^{\mathrm{T}} \left[{T^{(e)}}^{\mathrm{T}} S^{(e)}(\omega) T^{(e)} \right] A^{(e)} \tag{8}$$

$$S_s(\omega) u = 0 \iff \det\big(S_s(\omega)\big) = 0 \tag{9}$$

In practice, due to the high sensitivity of $S_s(\omega)$, it is numerically more robust to track the smallest singular value $\sigma_{min}\big(S_s(\omega)\big)$ or use methods such as the Wittrick–Williams algorithm, avoiding cancellation errors and ensuring accurate identification of the natural frequencies. Typical visualizations include plots of $\log\|\det\big(S_s(\omega)\big)\|$ or $\sigma_{min}\big(S_s(\omega)\big)$ versus frequency, where sharp minima indicate the structure's natural frequencies [18]. This framework provides a highly efficient and accurate representation of prestressed tensegrity members, capturing both axial and transverse dynamics while naturally accommodating rigid-body modes, prestress effects, and frequency-dependent behavior. This complete formulation ensures full reproducibility of the computational model and code is available in repository.

2.1. Validation of the Spectral Element Method (SEM)

The SEM formulation was implemented in MATLAB and applied to tensegrity topologies, namely the X-Module, 3-Strut Simplex, 4-Strut Simplex, Truncated Tetrahedron, and Expanded Octahedron. The models were simulated using the same geometric dimensions and prestress levels in the compressive members, allowing direct comparison with the reference study. The resulting spectral responses are shown in Fig. 3, where $\log\|\det\big(S_s(\omega)\big)\|$ is plotted against frequency. The minima correspond to the natural frequencies of each structure, and the curves reproduce the characteristic responses reported by Gan and Kiryu [18].

This approach offers a direct alternative to conventional finite element homogenization methods, enabling the explicit derivation of effective elastic properties for tensegrity structures with arbitrary topologies. Its validity has been verified across various modular cases, as discussed in the results and simulations section. Figure 3 illustrates the directional stiffness derived from the computed elasticity tensor for three representative topologies from the literature. The figure reveals how each configuration inherently exhibits directional behavior, ranging from anisotropic to isotropic stiffness distributions, even under stable structural arrangements. Furthermore, it highlights how topological variations can significantly alter the directional rigidity, underscoring the importance of geometry in determining the mechanical response of tensegrity cells.

To further validate the proposed SEM formulation, a quantitative comparison was performed against classical Finite Element Method (FEM) models using equivalent geometric and prestress conditions. Table 1 summarizes the first six natural frequencies obtained for five tensegrity configurations. These results serve to assess the accuracy of the spectral model in reproducing the fundamental and higher-order vibration modes without resorting to fine discretization. The FEM solutions were computed using standard 3D truss elements with sufficient mesh refinement, while the SEM results were obtained with only one spectral element per member, demonstrating its high numerical efficiency.

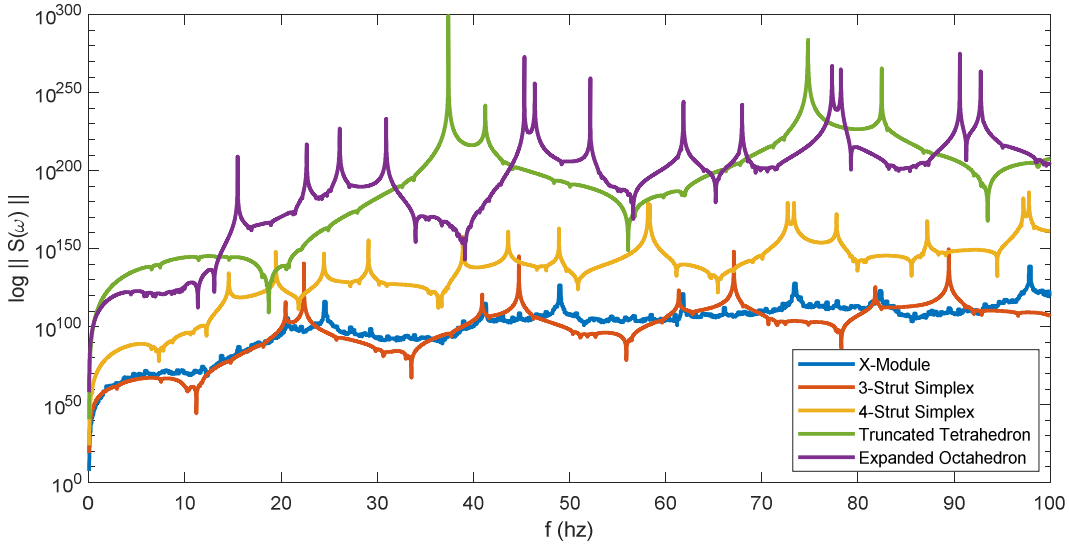

Fig. 3. Spectral response $\log\|\det(S_s(\omega))\|$ versus frequency for tensegrity topologies. The plots were obtained using identical dimensions and prestress values as in Gan & Kiryu [18] for direct validation.

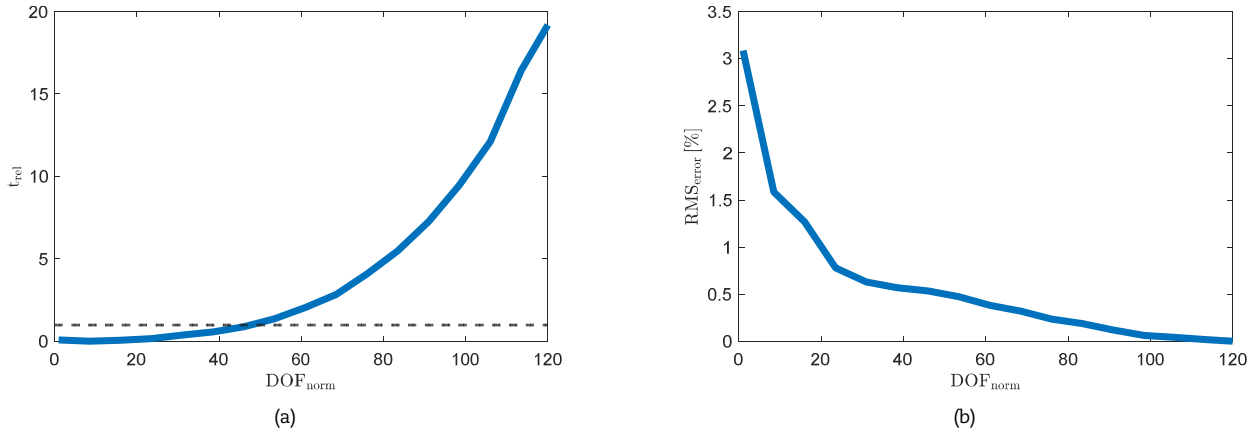

Fig. 4. Convergence and efficiency comparison between FEM and SEM: (a) relative computational time versus normalized DOF, (b) RMS error versus normalized DOF.

To complement this frequency-level comparison, an additional benchmark was conducted across all topologies to quantify the convergence and computational efficiency of both methods. The results, presented in Fig. 4, describe the relationship between accuracy, degrees of freedom, and computational time. The plots employ a normalized degree-of-freedom measure defined as $\mathrm{DOF}_{\mathrm{norm}} = \mathrm{DOF}_{\mathrm{FEM}}/\mathrm{DOF}_{\mathrm{SEM}}$, where $\mathrm{DOF} = 3 \times N_{\mathrm{nodes,free}}$ denotes the total number of active degrees of freedom. The computational cost is expressed as a relative time $t_{\mathrm{rel}} = \mathrm{time}_{\mathrm{FEM}}/\mathrm{time}_{\mathrm{SEM}}$. Both t_{rel} and the RMS error of the first six natural frequencies were averaged over the selected topologies to produce representative, topology-independent trends. The RMS error values were computed mode-by-mode, aggregated, and normalized consistently for all cases. A dashed line at $t_{\mathrm{rel}} = 1$ is included in Fig. 4(a) to indicate the threshold where FEM and SEM require equal CPU time.

The benchmark reveals clear tendencies: the computational time increases exponentially as $\mathrm{DOF}_{\mathrm{norm}}$ grows, grows, while the RMS error decreases exponentially with FEM mesh refinement. The intersection point where FEM and SEM present comparable computational time occurs at approximately $\mathrm{DOF}_{\mathrm{norm}} \approx 48$, for which the global RMS error relative to the SEM reference is approximately 0.53%. These results confirm that the SEM achieves high accuracy with substantially fewer degrees of freedom and without the need for fine FEM discretization. The patterns observed in Fig. 4 are consistent with the frequency comparisons in Table 1, reinforcing the effectiveness of the spectral formulation.

Table 1. Comparison of the first six natural frequencies obtained using FEM and SEM for different tensegrity structures.

Structure Type	Method	f_1 (Hz)	f_2 (Hz)	f_3 (Hz)	f_4 (Hz)	f_5 (Hz)	f_6 (Hz)
X-Module	FEM	9.227	15.166	18.741	22.48	27.324	33.489
	SEM	9.21	15.05	18.65	22.6	27.1	33.7
3-Strut Simplex	FEM	9.856	12.058	15.45	16.901	33.689	36.193
	SEM	10.19	11.79	14.74	18.14	33.54	37.66
4-Strut Simplex	FEM	6.769	8.652	9.911	13.638	23.893	27.631
	SEM	6.98	8.69	10.56	12.22	21.8	27.18
Truncated Tetrahedron	FEM	12.249	19.694	20.042	28.717	32.578	36
	SEM	11.41	18.7	20.54	27.91	32.59	35.8
Expanded Octahedron	FEM	6.457	11.533	17.1	19.12	21.569	24.494
	SEM	5.75	11.32	16.9	18.92	21.44	24.91

The agreement between FEM and SEM results is excellent across all cases, with average discrepancies below 3% for the first six natural frequencies and maximum deviations below 6% in higher modes. This confirms that the SEM reproduces the essential dynamic behavior of tensegrity systems with remarkable precision using far fewer degrees of freedom. These observations are consistent with the spectral responses illustrated in Fig. 4, where the SEM captures all resonance peaks with high fidelity compared to the FEM reference. The small deviations observed at higher frequencies are expected, as SEM computes exact member-level dynamics while FEM results depend on mesh density and polynomial interpolation. The SEM offers several advantages for tensegrity systems: (i) it incorporates axial prestress and its geometric effects directly into the dynamic stiffness; (ii) it requires fewer degrees of freedom than a finely discretized FEM to capture equivalent spectral responses; and (iii) it naturally handles free-vibration problems in structures without supports, since detecting singularities in $S_s(\omega)$ reveals both rigid-body modes and internal mechanisms.

3. Dynamic Objective Functions for Optimization

Building upon the Spectral Element Method (SEM) formulation presented in the previous section, this section introduces the dynamic objective functions that drive the optimization process of tensegrity unit cells. These functions are defined directly from the spectral response of the structure, obtained through the frequency-dependent stiffness formulation derived earlier. The main objective of the optimization is to enhance the effective elastic and dynamic performance of the tensegrity structure by systematically modifying its geometry, connectivity topology, and prestress distribution. To achieve this, a set of five scalar objective functions is proposed, each targeting a distinct mechanical or dynamic criterion relevant to the behavior of prestressed tensegrity systems.

These functions quantify different aspects of vibrational efficiency, modal distribution, robustness to prestress variations, and resistance to external excitation. Each one is treated in an independent optimization run to produce specialized tensegrity configurations tailored to specific design objectives. The resulting configurations are subsequently compared to assess trade-offs among stiffness, stability, isotropy, and dynamic resilience. The five objective functions considered are described as follows:

1. Dynamic Efficiency (DE): Defined in Eq. (10), maximizes the ratio between the fundamental natural frequency ω_1 and the total mass M. This objective provides a normalized measure of dynamic stiffness, allowing fair comparison between topologies of different sizes or masses. A higher DE value indicates a configuration that is both lightweight and dynamically stiff, optimizing the fundamental vibrational performance of the tensegrity cell:

$$DE = \frac{\omega_1}{M} \tag{10}$$

2. Minimum Modal Separation (MMS): As expressed in Eq. (11), this metric evaluates the minimum frequency spacing among the first k natural frequencies. Larger MMS values correspond to well-separated modes, reducing the likelihood of modal coupling and resonance overlap under broadband excitations. This objective is particularly relevant in tensegrity lattices where multiple close-lying frequencies can compromise dynamic performance:

$$MMS = \min_{j=1,\ldots,k-1} (\omega_{j+1} - \omega_j) \tag{11}$$

3. Modal Density Ratio (MDR): This objective, expressed in Eq. (12), quantifies the concentration of vibration modes below a predefined cutoff frequency ω_{max}. It is computed as the ratio between the number of modes with $\omega_j < \omega_{max}$ and the cutoff frequency itself. Minimizing MDR promotes sparser low-frequency modal distributions and higher overall stiffness, thereby reducing the likelihood of unwanted low-frequency resonances. This metric is useful for designing tensegrity cells intended to maintain dynamic stability across a broad frequency range:

$$MDR = \frac{N_{\omega_j < \omega_{max}}}{\omega_{max}} \tag{12}$$

4. Prestress Robustness (PR): Defined in Eq. (13), this function quantifies the sensitivity of the fundamental frequency ω_1 to perturbations in the self-stress vector q. It is computed as the standard deviation of ω_1 under random variations of the prestress state. Minimizing PR ensures that the tensegrity structure remains stable and predictable under manufacturing tolerances or operational variations in prestress, which is critical for deployable or load-sensitive applications:

$$PR = std\big(\omega_1(q + \delta q)\big) \tag{13}$$

5. Critical FRF Magnitude (CFM): As shown in Eq. (14), this metric measures the maximum amplitude of the frequency response function (FRF) within a specified critical frequency band Ω_{crit}. It is obtained by applying a unit excitation and monitoring the global displacement response. By minimizing CFM, large vibration amplitudes under external excitations are avoided, enhancing the dynamic resilience of the structure:

$$CFM = \max_{\omega \in \Omega_{\text{crit}}} |u(\omega)| \tag{14}$$

Each of these objective functions is optimized individually using the same numerical framework. This single-objective optimization strategy allows the identification of tensegrity topologies tailored to specific performance criteria, while facilitating the comparison of trade-offs among stiffness, isotropy, prestress sensitivity, and directional balance. The selection of these distinct functions reflects both the versatility and complexity of tensegrity structures and supports their rational design for targeted engineering applications.

4. Optimization Methodology

This section describes the computational framework employed to optimize the tensegrity structures using the dynamic objectives previously defined. Building upon the spectral formulation developed, the optimization process aims to identify geometrical and topological configurations that enhance the dynamic performance of tensegrity unit cells. To explore this high-dimensional nonlinear landscape effectively, a Particle Swarm Optimization (PSO) algorithm is employed. The following subsections detail the PSO implementation, the stability verification procedure, and the simulation setup used for the case studies considered in this work.

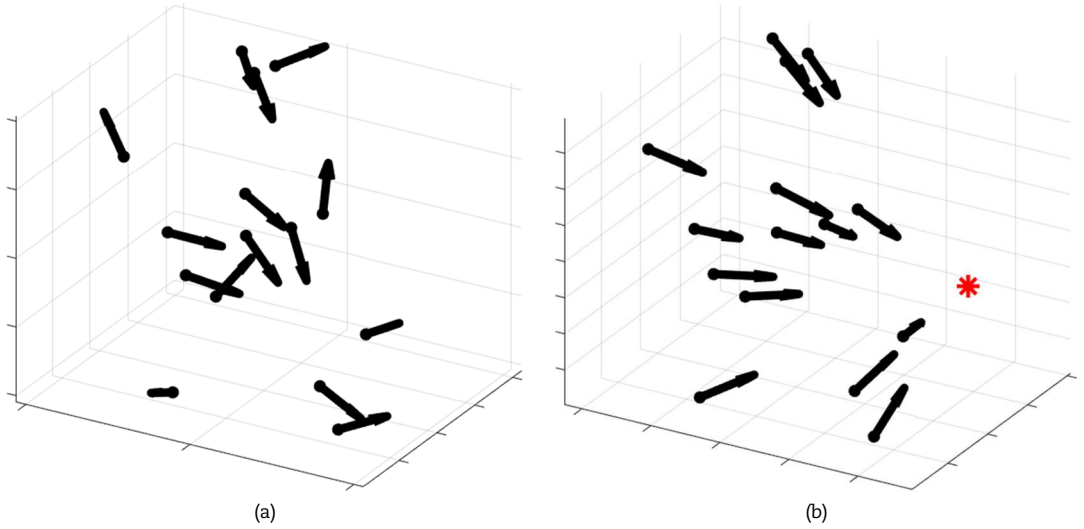

Fig. 5. Particle dynamics and convergence behavior in PSO.

4.1. Particle Swarm Optimization (PSO)

The search for optimal tensegrity configurations with enhanced dynamic and elastic behavior demands a numerical strategy capable of exploring large and multimodal design spaces while maintaining computational efficiency. Among available population-based techniques, the Particle Swarm Optimization (PSO) algorithm has proven particularly effective for such nonlinear problems. In this approach, a group of interacting agents (called particles) moves collectively through the design domain, each particle representing a candidate tensegrity geometry defined by the nodal coordinates of the unit cell. The design variable vector associated with the i-th particle is denoted as $x_i \in R^{3n_n}$ where n_n is the number of nodes, and each node has three spatial coordinates (x, y, z). Hence, the dimensionality of the search space is $n_{\text{var}} = 3n_n$. Each particle also possesses a velocity vector v_i of the same dimension, which determines how its position evolves from one iteration to the next.

The standard PSO update mechanism is expressed as in Eq. (15), where www is the inertia weight controlling the memory of the particle's previous motion, c_1 and c_2 are the cognitive and social acceleration coefficients, and $r_1, r_2 \in [0,1]$ are random scalars introducing stochastic variability. The vectors p_i and g denote, respectively, the best position previously visited by particle i and the best position found by the entire swarm. The position update is then performed by Eq. (16):

$$v_i^{t+1} = w.\, v_i^t + c_1.\, r_1.\, (p_i - x_i^t) + c_2.\, r_2.\, (g - x_i^t) \tag{15}$$

$$x_i^{t+1} = x_i^t + v_i^{t+1} \tag{16}$$

This process continues iteratively until a stopping condition is satisfied, such as reaching the maximum number of iterations or detecting convergence of the objective function. The combined action of the inertial, cognitive, and social terms allows the swarm to balance exploration (searching broadly in the design space) and exploitation (refining promising solutions). Figure 5 schematically illustrates this behavior. In Fig. 5(a), particles are initialized at random positions with arbitrary velocities in a multidimensional space representing all possible tensegrity configurations. Over successive iterations, as in Fig. 5(b), particles adjust their trajectories toward the global optimum (indicated by a red star) guided by both individual experience p_i and collective learning g. This dynamic interaction promotes self-organization and cooperative convergence, key features that make PSO suitable for identifying high-performance tensegrity layouts with minimal computational effort.

The swarm evolution proceeds iteratively until a convergence criterion is satisfied, typically when the improvement in the objective function becomes negligible or when the algorithm reaches a predefined iteration limit. In this work, a parallelized PSO implementation was adopted to accelerate convergence and enhance exploration capabilities. The adopted parameter configuration and admissible domain are summarized in Table 2, whose values were selected following established guidelines to achieve a balanced compromise between global exploration and local refinement within the multidimensional design space. All nodes are allowed to move freely in the three spatial directions, and the connectivity matrix preserves the underlying topology. To prevent rigid-body drift, the centroid of each particle configuration is re-centered at every iteration.

During each iteration, particles are monitored to ensure that their positions remain within the admissible geometric limits. If a particle crosses the predefined search boundaries, a velocity reflection mechanism is applied: the offending velocity component is reversed in sign, and the position is reprojected back into the feasible region. This corrective procedure prevents divergence of the swarm and maintains the physical admissibility of all candidate tensegrity geometries throughout the optimization process.

An essential stage in the optimization workflow is the stability verification of each proposed tensegrity configuration. Prior to evaluation, all candidate geometries generated by the swarm are checked for self-equilibrium of the tensile and compressive members. Configurations that fail to satisfy the equilibrium conditions are automatically rejected, ensuring that only mechanically admissible tensegrity units participate in the optimization process. Moreover, the nodal coordinates of each cell are normalized to maintain consistent geometric scaling and avoid ill-conditioned configurations.

Table 2. Optimization parameters used in the PSO algorithm.

Parameter	Value	Parameter	Value
Number of particles n_{pop}	100	Inertia weight	1.0
Damping factor w_{damp}	0.99	Cognitive coefficient	1.5
Social coefficient	2.0	Position range	[–0.2, 0.2]
Velocity limits	±10% of position range	Stopping criterion	Improvement < 10^{-5} after 20 iterations

Table 3. Characteristics of the tensegrity topologies.

Topology ID	Number of Bars	Number of Cables	Number of Nodes
A	3	9	6
B	4	12	8
C	6	18	12
D	6	24	12

Table 4. Material and geometric properties of tensegrity elements.

Bar Parameter	Value	Cable Parameter	Value
Diameter [mm]	10	Diameter [mm]	2
Material	Structural steel	Material	Steel wire rope
Young's Modulus [GPa]	206.04	Young's Modulus [GPa]	75.999
Density ρ [kg/m³]	7870	Density ρ [kg/m³]	7870
Reference Internal Force [N]	100	–	–

To rigorously enforce structural stability, an additional constraint is introduced based on the projected stiffness Λ, defined in Eq. (17), which evaluates the response of the structure in the subspace associated with infinitesimal mechanisms. M denotes a basis of the null space of the equilibrium matrix A, that is, the space of nodal displacement patterns that do not induce first-order changes in member lengths and therefore correspond to potential mechanisms of the structure. Since stability under prestress is governed precisely by how the structure reacts along these mechanism directions, the stiffness matrix must be evaluated in this subspace rather than in the full kinematic space:

$$\Lambda = M^{\mathrm{T}}(I_3 \bigotimes D)M \succ 0 \tag{17}$$

The projected matrix Λ represents the tangent stiffness restricted to the mechanism-compatible subspace. The condition $\Lambda \succ 0$ implies that all admissible mechanism directions gain positive stiffness under the current level of self-stress, and thus no infinitesimal collapse or buckling mode is present. Numerically, this requirement is verified by computing the eigenvalues of Λ; only configurations for which all eigenvalues are strictly positive are retained as stable tensegrity candidates. This constraint effectively filters out geometries susceptible to buckling or loss of tension, ensuring that the final optimized topologies remain structurally viable under prestress.

4.2. Case of study and simulation setup

A total of 200 independent optimization runs were performed, combining four representative tensegrity topologies (A–D) with five distinct objective functions, each repeated ten times to ensure statistical robustness of the results. All simulations were executed in MATLAB R2024a on a 12-core i7-12700K CPU with 32 GB RAM. The geometric characteristics of the selected topologies are summarized in Table 3, including the number of struts, cables, and nodes that define each system. These configurations correspond to canonical tensegrity units widely analyzed in the literature, shown in Fig. 1, serving as reliable benchmarks for validating the proposed optimization framework. By subjecting each topology to different performance criteria, the study investigates how variations in nodal layout and connectivity pattern influence the mechanical behavior of the structure, providing a systematic basis for comparing stiffness, stability, and dynamic performance across designs.

The material and geometric parameters used for the tensegrity members are listed in Table 4. These constants were kept uniform throughout all simulations to ensure that differences in the outcomes stem solely from topology and optimization effects rather than from material variability. The selected values correspond to feasible dimensions for laboratory-scale tensegrity cells (≈20 × 20 × 20 cm). Struts were modeled using structural steel, while the cables were represented by high-strength steel wire rope, both with consistent density to maintain uniform mass distribution. The chosen prestress levels guarantee mechanical stability while remaining safely below the critical buckling threshold of the struts and the ultimate tensile strength of the cables. For instance, compressive members were preloaded between 200 and 300 N, roughly 20–30% of the Euler buckling limit for a 5 mm diameter strut, balancing stiffness and safety. The tensile elements carried pretensions of 80–160 N, which corresponds to cable diameters in the range of 0.6–0.8 mm, ensuring a well-distributed internal force network within each cell. This standardized setup provides a controlled environment to assess the effects of the optimization algorithm on the overall mechanical response, enabling consistent cross-comparison among all topological configurations.

5. Results and Discussion

A comprehensive PSO optimization campaign was carried out on the four tensegrity topologies, each evaluated with five vibration-oriented metrics. This section presents the results of those campaigns, organized around four topics: (i) convergence behavior (average trends and variability across independent runs), (ii) optimized equilibrium geometries for each topology–metric pair, (iii) distributions of internal forces, and (iv) frequency-response characteristics of the final designs. Results are reported using multiple independent optimization runs per case to assess repeatability and robustness. As an illustrative example, Fig. 6 shows the evolution of Topology A under the MDR objective: the five panels trace the progressive nodal adjustments from the initial layout to the final optimized configuration, highlighting how the swarm iteratively refines the topology to improve modal spacing. The subsections that follow provide quantitative and qualitative comparisons across topologies and objectives.

5.1. Convergence analysis

Figure 7 summarizes the convergence behavior of the PSO optimization across the four tensegrity topologies and the five objective metrics. Figure 7(a) shows the average normalized convergence histories for topologies A–D (f/f_0 versus iteration number). All topologies exhibit a rapid initial reduction of the objective function during the first 40–50 iterations, followed by slower refinement, indicating that PSO efficiently locates high-quality solution regions before reaching near-optimal configurations. Topology A converges the fastest and most consistently, achieving the lowest normalized value in fewer than 40 iterations, suggesting a smoother optimization landscape. Topologies B and C converge more slowly and stabilize at intermediate levels, reflecting higher sensitivity to design variables or the presence of multiple local minima. Topology D shows the most gradual convergence but ultimately reaches a competitive final value, highlighting a more complex yet robust search path. These trends confirm that both geometry and connectivity strongly influence convergence dynamics.

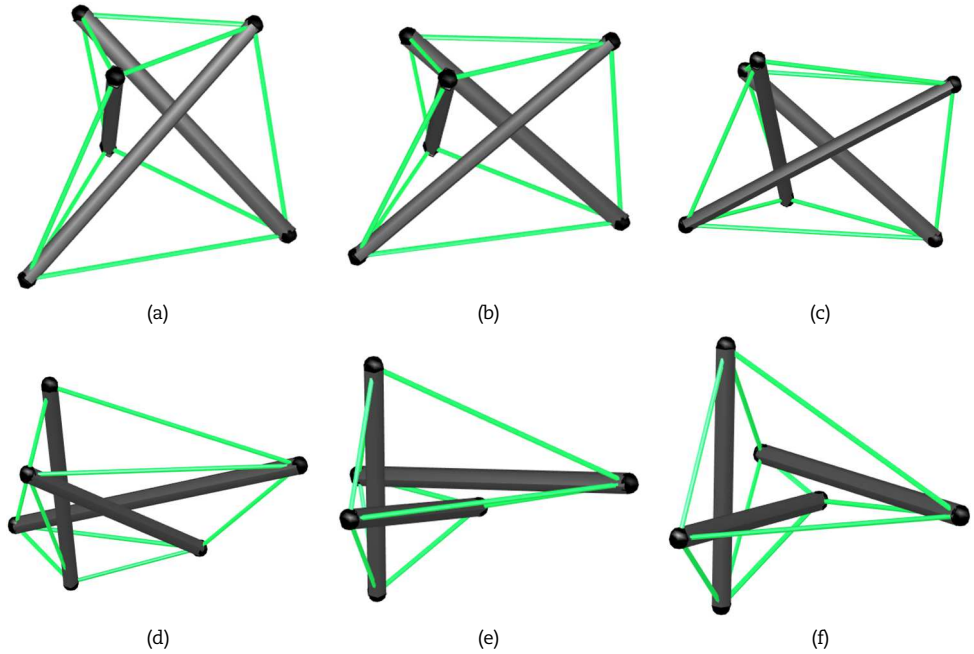

Fig. 6. Topology Evolution during PSO Optimization (Topology A – MDR Metric). Representative snapshots spanning the optimization.

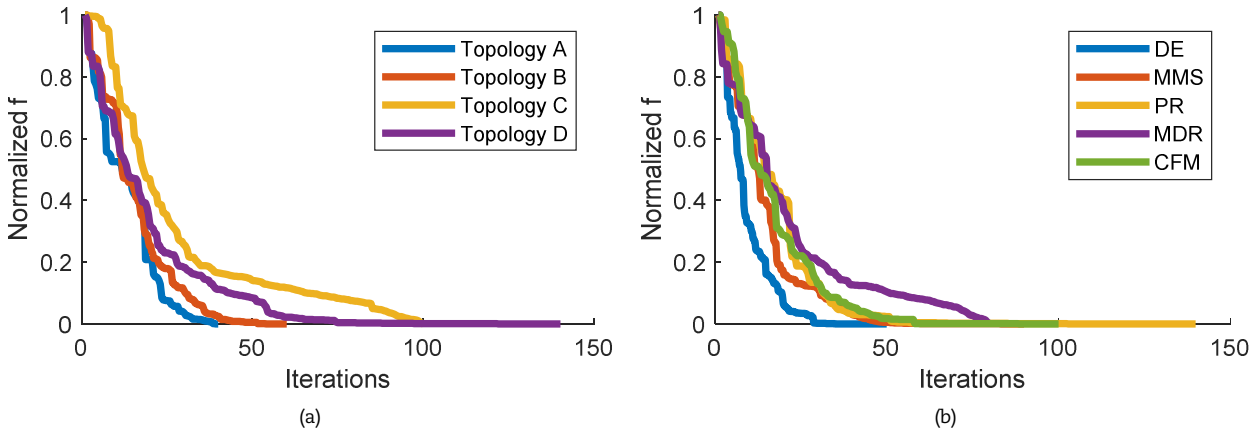

Fig. 7. Average normalized convergence: (a) by tensegrity topology, (b) by optimization metric.

Figure 7(b) presents the convergence histories grouped by metric and averaged across all topologies. DE converges fastest and reaches the lowest final value, consistent with a well-conditioned fitness landscape and clear sensitivity to beneficial design changes. MMS and CFM converge efficiently as well, although their final values are slightly higher. PR and MDR converge more slowly and exhibit greater variability, indicating more complex or less well-conditioned objective surfaces. Metrics sensitive to modal spacing or prestress variations (MDR, PR) may require parameter tuning, increased population size, or hybrid optimization strategies to achieve comparable performance. Overall, the analysis demonstrates that both topology and metric selection critically affect optimization efficiency. Metrics related to stiffness and dynamic energy (DE, CFM) provide rapid and reliable convergence, whereas modal- and robustness-oriented metrics (MDR, PR) demand careful configuration. These insights highlight the importance of selecting appropriate objectives and considering the geometric complexity of tensegrity topologies in metaheuristic optimization campaigns.

5.2. Optimized configurations

Figure 8 shows the optimized equilibrium configurations of Topology A for the five considered metrics: DE, MMS, MDR, PR, and CFM (from left to right). DE and PR preserve nearly orthogonal bar arrangements, reflecting geometrically regular and mechanically balanced tensegrity states with uniform prestress distribution. These solutions indicate that objectives related to stiffness and prestress robustness tend to favor symmetric and globally coherent structures, suggesting that certain optimization targets naturally reinforce structural regularity. MMS and MDR retain the X-module pattern but introduce slight inclinations, enhancing modal separation while moderately reducing geometric symmetry. This adjustment demonstrates how modal-oriented objectives can induce subtle yet meaningful changes in bar orientations and self-stress, optimizing dynamic performance without drastically compromising structural balance.

CFM departs subtly from the X-aligned families, adjusting compressive and tensile members to improve frequency-response stability rather than geometric uniformity. This configuration highlights the trade-off between achieving optimal vibrational behavior and maintaining strict symmetry, illustrating how frequency-focused objectives may prioritize dynamic criteria over purely geometric considerations. Overall, these results illustrate the sensitivity of tensegrity systems to the chosen objective: even within a single topology, distinct metrics lead to unique equilibrium configurations and self-stress distributions, emphasizing the importance of careful metric selection in the design process and the need to consider the intended functional priorities when guiding optimization.

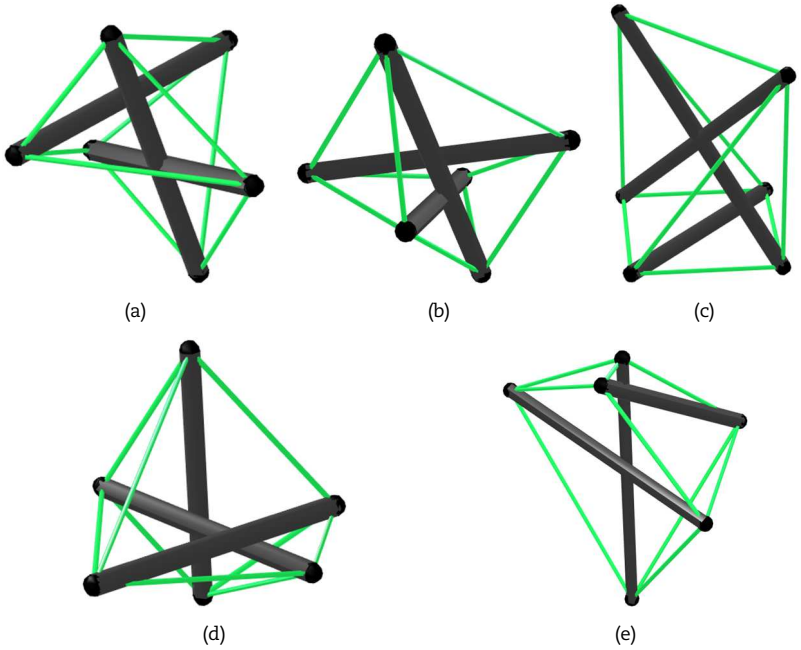

Fig. 8. Optimized Configurations of Topology A.

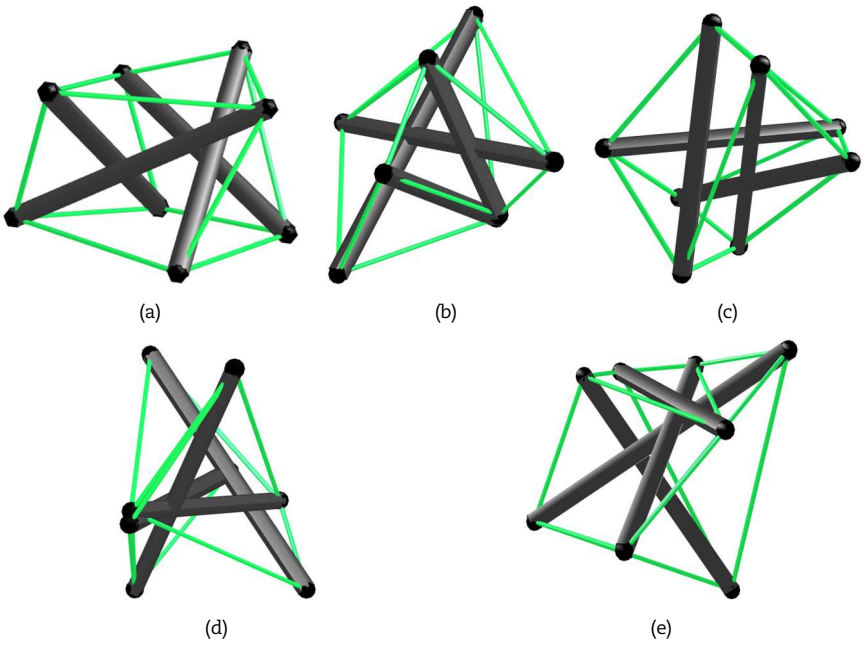

Fig. 9. Optimized Configurations of Topology B.

Figure 9 shows the optimized equilibrium configurations for Topology B under the five metrics: DE, MMS, MDR, PR, and CFM. With a higher number of members than Topology A, Topology B presents a broader design space, allowing for more complex equilibrium shapes and diverse stress redistributions. DE and MDR preserve geometric symmetry and maintain balanced prestress distributions, producing configurations that optimize stiffness and modal efficiency while keeping the overall structural layout coherent. These solutions indicate that objectives related to stiffness and modal performance continue to favor mechanically robust and regular structures even as the topology becomes more intricate.

MMS introduces moderate asymmetry by slightly reorienting bars and suppressing a tensile element, leading to a compact, class-2-like configuration that enhances modal separation without drastically compromising structural balance. PR, on the other hand, drives the system toward diagonal X-shaped arrangements, merging nodes and prioritizing prestress robustness at the expense of geometric uniformity. CFM adjusts compressive and tensile members to improve frequency-response stability, resulting in configurations that are less symmetric but better suited for dynamic control, highlighting the trade-offs between vibrational optimization and topological regularity.

Overall, Topology B demonstrates increased sensitivity to the selected optimization metric due to its additional degrees of freedom. While DE and MDR consistently produce balanced and mechanically coherent configurations, MMS, PR, and CFM explore dynamically favorable or robustness-oriented arrangements. These results underscore the fundamental trade-off in complex tensegrity systems between geometric regularity, prestress distribution, and functional performance, emphasizing that even within a single topology, the choice of objective function can substantially influence the resulting equilibrium configuration.

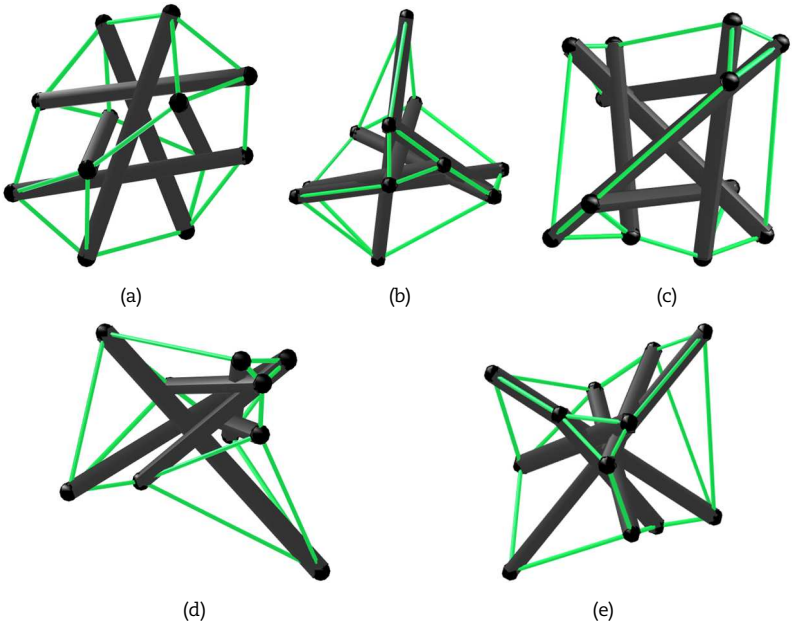

Fig. 10. Optimized Configurations of Topology C.

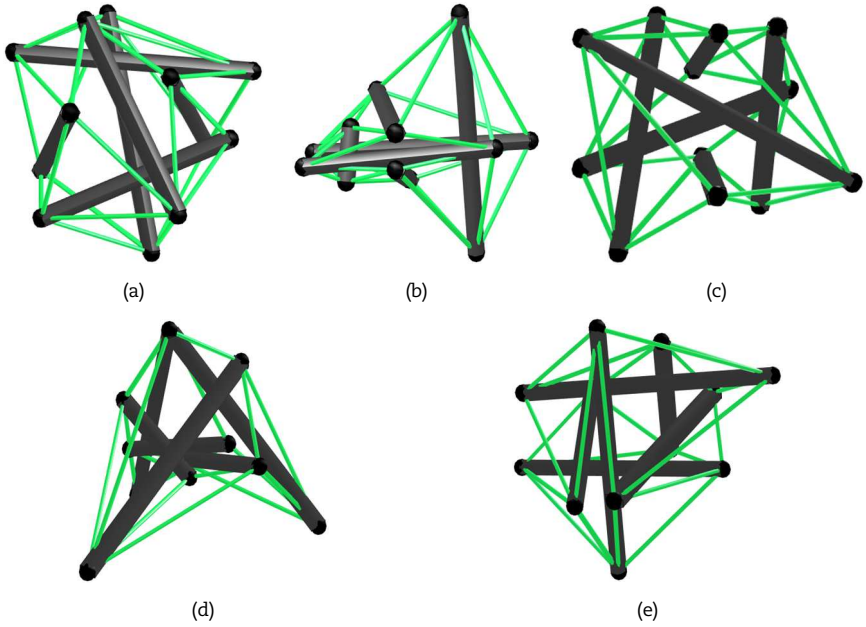

Fig. 11. Optimized Configurations of Topology D.

Figure 10 shows the optimized equilibrium configurations for Topology C under the five metrics: DE, MMS, MDR, PR, and CFM (from left to right). Due to its tetrahedron-based structure, Topology C exhibits higher geometric redundancy and a broader range of stable self-stress states than Topologies A and B. DE and MDR preserve the main geometric features of the canonical icosahedron while introducing slight shear deformations and mild rotations, respectively, to enhance global stiffness and modal distribution. These solutions demonstrate that objectives related to stiffness and modal performance naturally favor symmetric and mechanically coherent structures, even in topologies with increased connectivity and complexity.

In contrast, MMS produces elongated struts and localized node clustering, reflecting a strategy that prioritizes modal separation through moderate geometric adjustments. PR generates fewer uniform arrangements with concentrated compressive elements and overlapping cables, emphasizing prestress robustness but reducing global geometric regularity. CFM promotes inward contraction of the module, elongating tensile members and adjusting compressive elements to enhance frequency-response stability at the expense of isotropy. Overall, Topology C highlights the trade-off between maintaining structural symmetry and achieving specific dynamic or robustness-oriented objectives. The results illustrate that, in highly connected tensegrity systems, even small variations in the optimization target can lead to substantially different equilibrium shapes and prestress distributions, emphasizing the sensitivity of complex topologies to the choice of performance metric.

Figure 11 presents the optimized equilibrium configurations for Topology D under the five metrics: DE, MMS, MDR, PR, and CFM. As the most intricate topology considered, Topology D combines expanded octahedral geometry with additional members, offering a highly connected system with multiple stable self-stress states. DE and CFM preserve the overall geometric symmetry of the canonical structure, introducing only minor rotations and subtle node displacements to enhance global stiffness and maintain a coherent prestress distribution. These solutions illustrate that objective targeting stiffness or frequency-response stability naturally favor mechanically balanced and symmetric configurations, even in topologies with high connectivity.

Table 5. Performance metrics of optimized tensegrity structures and robustness of PSO optimization results.

Topology ID	Optimized Metric	Value of Optimized Metric	Std (est)	% Variation
A	DE	-145.3	6.76	4.7%
A	MMS	-30.90	2.41	7.8%
A	MDR	0.05	0.004	8.0%
A	PR	0.004104	6.62e-04	16.1%
A	CFM	95.79	7.12	7.4%
B	DE	-132.4	10.4	7.9%
B	MMS	-35.80	3.52	9.8%
B	MDR	0.035	0.003	8.6%
B	PR	0.003078	4.07e-04	13.2%
B	CFM	136.7	11.7	8.5%
C	DE	-132.2	11.3	8.6%
C	MMS	-35.10	5.82	16.6%
C	MDR	0.035	0.003	8.6%
C	PR	0.007678	1.24e-03	16.1%
C	CFM	258.7	34.7	13.4%
D	DE	-51.69	7.65	14.8%
D	MMS	-10.00	1.58	15.8%
D	MDR	0.1	0.009	9.0%
D	PR	0.005712	9.60e-04	16.8%
D	CFM	206.6	30.1	14.6%

In contrast, MMS produces a more compact and anisotropic configuration by shortening select compression members and aligning several struts in parallel, emphasizing modal separation and local stiffness at the expense of perfect symmetry. MDR drives the structure toward moderate inclinations of the compression members while maintaining the connectivity pattern, balancing prestress redistribution with the preservation of overall geometry. PR leads to a pyramidal arrangement, where nodes are drawn closer, creating diagonally aligned struts and a configuration that prioritizes prestress robustness over geometric uniformity. Overall, Topology D demonstrates that even within a single, highly connected topology, the choice of optimization metric can result in distinct equilibrium shapes and prestress distributions. These results emphasize the trade-offs between structural regularity, functional adaptability, and dynamic performance, highlighting the sensitivity of complex tensegrity systems to the selected design objective.

Overall, the analysis of Topologies A through D demonstrates that tensegrity systems exhibit a strong sensitivity to the chosen optimization metric. Objectives related to stiffness and prestress robustness, such as DE and MDR, consistently favor symmetric, mechanically balanced configurations across all topologies, preserving geometric regularity even as connectivity and complexity increase. In contrast, metrics targeting modal separation, frequency-response control, or prestress robustness—represented by MMS, PR, and CFM—tend to induce moderate asymmetries, local rearrangements of bars, and variations in self-stress distribution, reflecting a deliberate trade-off between dynamic performance, robustness, and structural uniformity. These results highlight a fundamental principle in tensegrity design: even small changes in the optimization objective can produce markedly different equilibrium configurations, emphasizing the importance of selecting metrics that align with the intended functional priorities of the structure.

5.3. Performance assessment

Table 5 presents the optimized values of the five performance metrics, together with their estimated standard deviations and relative variations, allowing a joint evaluation of the optimization quality and robustness of the PSO procedure. A first observation is that metrics associated with stiffness and dynamic energy, such as DE and CFM, exhibit the lowest relative dispersion (below 9% in all topologies), confirming that these objectives define smoother and more well-behaved search landscapes. The PSO algorithm consistently converged toward stable optima for these metrics, suggesting that the underlying design space contains well-defined valleys with minimal local minima interference. Conversely, PR and MMS show markedly higher variability, frequently exceeding 15%, indicating that these metrics are more ill-conditioned or multi-modal, likely due to their dependence on higher-order nonlinear relationships between geometry, self-stress, and modal stiffness. In such cases, the optimizer must balance exploration and exploitation under a highly irregular objective surface, where small perturbations in nodal geometry or pretension can significantly affect the computed metric values.

The larger dispersion observed for MMS and PR, particularly in the more complex topologies, can be physically explained by the stronger coupling between geometry, prestress, and modal behavior. Metrics such as MMS and PR depend on higher-order quantities (modal curvatures, frequency ratios, and force–mode interactions) that are extremely sensitive to small geometric changes. In highly connected cells (Topologies C and D), a small perturbation in a single member length or pretension redistributes forces globally, altering multiple modal paths simultaneously. By contrast, DE and CFM depend primarily on low-order stiffness properties that vary smoothly with geometry, producing well-conditioned search spaces and lower variability. Thus, the increasing dispersion across topologies and metrics is a direct mechanical consequence of higher geometric redundancy, stronger modal coupling, and the nonlinear dependence of certain vibration metrics on the internal force state.

A second relevant observation is the systematic degradation of robustness with increasing topological complexity, as seen when moving from topology A to D. This trend evidences that more intricate tensegrity configurations generate stronger couplings between mechanical response and geometric degrees of freedom, thereby increasing the dimensionality and ruggedness of the optimization space. Despite this, PSO demonstrated remarkable adaptability, achieving acceptable convergence even for metrics with high intrinsic sensitivity. The comparative analysis across objectives suggests that DE and CFM constitute the most reliable and physically consistent optimization targets, while MDR and PR, though less robust, capture important vibrational features related to modal density and stiffness proportionality. These results highlight that optimization robustness is strongly tied to the conditioning and scale of each metric, and that metaheuristic frameworks like PSO remain effective when properly tuned, although future work could benefit from hybrid or regularized strategies to stabilize convergence for highly nonlinear metrics.

Table 6. Sensitivity of fundamental modal frequencies to perturbations for representative tensegrity topologies.

Structure Type	std_q (Hz)	CV_q (%)	std_l (Hz)	CV_l (%)	std_{EA} (Hz)	CV_{EA} (%)
X-Module	0.28	1.33	0.42	2.00	0.33	1.57
3-Strut Simplex	0.22	1.05	0.38	1.81	0.26	1.24
4-Strut Simplex	0.25	1.72	0.72	4.94	0.68	4.67
Truncated Tetrahedron	0.30	1.22	0.11	0.45	0.10	0.41
Expanded Octahedron	0.34	2.06	0.56	3.39	0.44	2.66

A Monte Carlo uncertainty analysis (N = 1000 samples per case) was performed to quantify the sensitivity of the first six natural frequencies to 5% multiplicative perturbations applied independently to the self-stress vector q, member lengths l, and the axial stiffness EA. For each realization, the SEM solver computed the six lowest modes, from which the standard deviation std and the coefficient of variation CV were evaluated per topology. These variance-based summary statistics demonstrate that the observed dispersion in the optimization results is due to the physical sensitivity of each topology to input uncertainty rather than numerical artifacts. The data further indicate that perturbations in l produce the largest variability in highly connected cells (e.g., 4-Strut and Expanded), while changes in q and EA typically have milder effects (see Table 6).

Figure 12 presents the frequency response of the optimized tensegrity structures for the DE and MMS metrics, expressed as the logarithmic magnitude of the spectral norm $\|S(\omega)\|$ over the frequency range from 0 to 200 Hz. The results reveal distinct patterns that relate dynamic performance to both the chosen optimization metric and the structural complexity of each topology. Under DE-based optimization (Fig. 12(a)), simpler configurations (Topologies A and B) exhibit compact and bounded frequency spectra, indicating enhanced dynamic stability and effective damping. Topology B shows slightly higher spectral amplitudes than A, suggesting that additional members introduce minor resonance channels, though overall spectral compactness is maintained. In contrast, the more complex lattices (Topologies C and D) display progressively larger frequency responses. Topology C exhibits intermediate growth with pronounced peaks around 50 Hz and above 120 Hz, whereas Topology D shows the steepest increase, spanning several orders of magnitude. These trends reflect the broader design space and higher degrees of freedom in complex topologies, which, while advantageous for static load redistribution, generate multiple high-frequency resonances.

The MMS-optimized structures (Fig. 12(b)) reveal similar distinctions. Topologies A and B maintain low spectral growth with smooth curves, with Topology A achieving the most compact spectrum—at least three orders of magnitude below the high-frequency amplitudes of the complex topologies. Topologies C and D, however, exhibit amplified responses across the frequency range, with extreme peaks near the upper limit. This indicates that MMS optimization, although effective in enhancing modal separation and redistributing internal stresses, favors configurations that are more sensitive to dynamic excitation in highly connected lattices. Overall, the frequency response analysis highlights two key insights. First, the optimization metric strongly influences dynamic characteristics, with DE favoring spectral compactness and MMS enhancing modal separation. Second, topological complexity modulates susceptibility to high-frequency resonances, establishing a clear trade-off between static optimization efficiency and vibrational robustness. Simpler topologies (A and B) consistently achieve compact, stable spectra, whereas more complex lattices (C and D) display richer but less controllable dynamic responses.

Figure 13 presents the frequency response of the optimized tensegrity structures for the Modal Density Ratio (MDR) and Prestress Robustness (PR) metrics. The results reveal how dynamic performance is influenced by both the chosen optimization criterion and the structural complexity of each topology. Under MDR optimization (Fig. 13(a)), simpler configurations (Topologies A and B) display compact and stable spectra. Topology A exhibits the lowest spectral growth and minimal resonance peaks, reflecting effective modal sparsity and enhanced global stiffness. Topology B follows a similar pattern, with slightly higher amplitudes, suggesting that the additional nodal connections introduce well-separated modal contributions without compromising overall spectral compactness. In contrast, the more complex lattices (Topologies C and D) show substantially amplified responses, particularly above 100 Hz, with multiple resonant peaks. This behavior indicates that denser connectivity and geometric complexity lead to stronger mode coupling, making high-frequency resonances more pronounced.

PR-based optimization (Fig. 13(b)) shows a comparable hierarchy among the topologies, but through a different mechanism. Topology A maintains the lowest and most uniform spectral amplitudes, demonstrating high dynamic stability and minimal sensitivity to prestress variations. Topology B exhibits slightly higher amplitudes, highlighting a trade-off between robustness and flexibility.

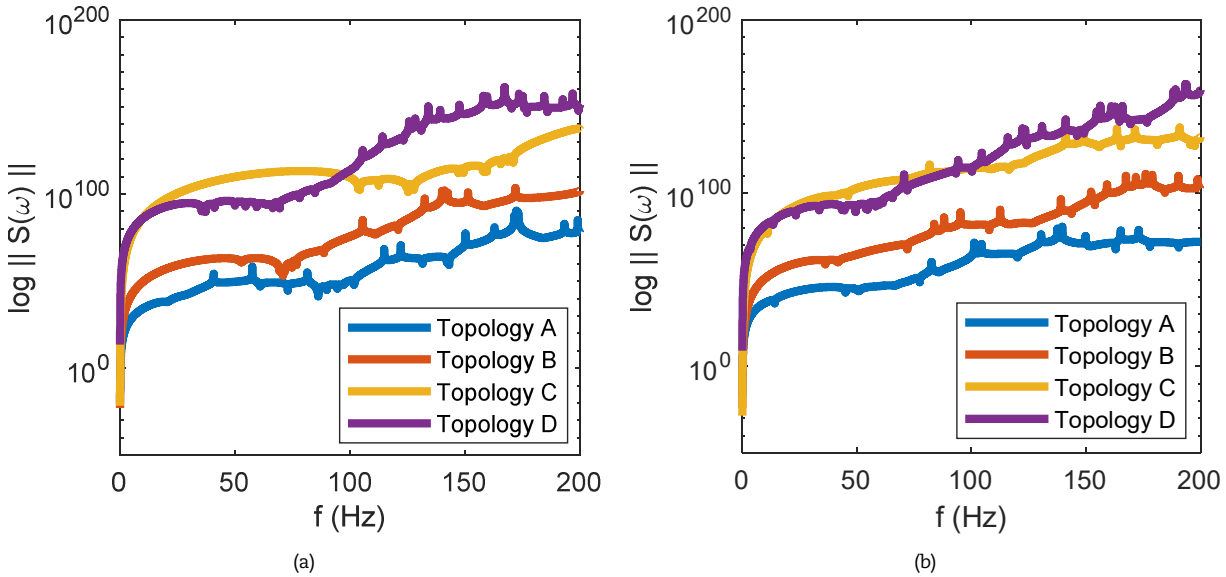

Fig. 12. Frequency response of optimized tensegrity structures for vibration metrics, (a) Optimizing DE, (b) Optimizing MMS.

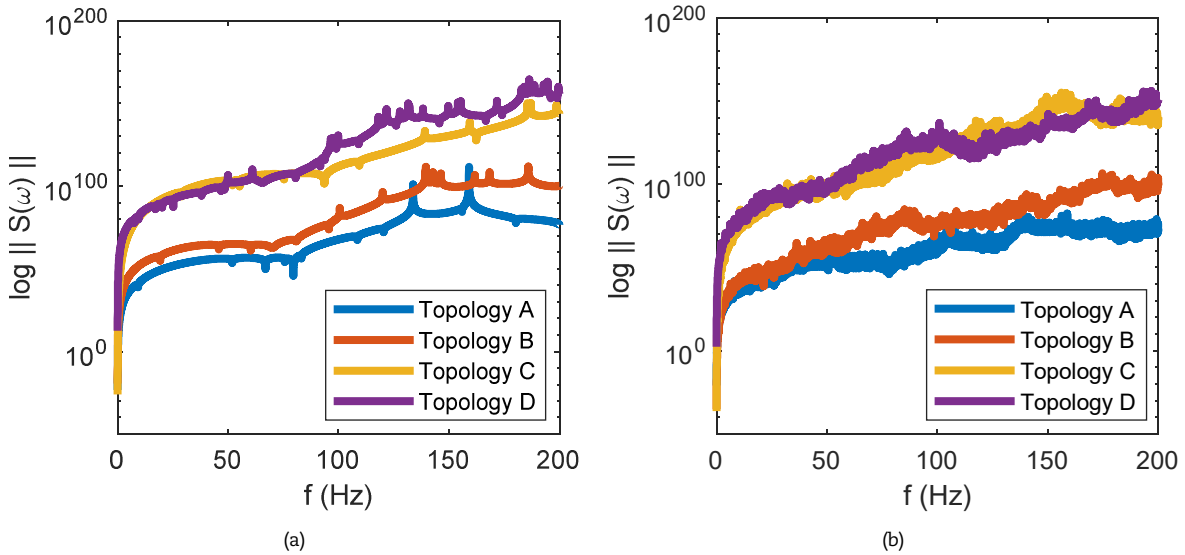

Fig. 13. Frequency response of optimized tensegrity structures for vibration metrics, (a) Optimizing MDR, (b) Optimizing PR.

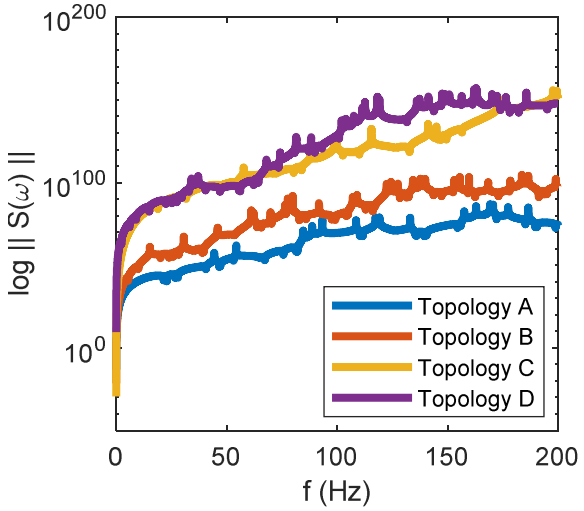

Fig. 14. Frequency response of optimized tensegrity structures for vibration metrics optimizing CFM.

In contrast, Topologies C and D experience steep spectral growth and irregular fluctuations, reflecting increased sensitivity to prestress perturbations and stronger modal interactions. These trends indicate that highly connected systems are more susceptible to local instabilities when internal forces deviate from equilibrium. Overall, the analysis of MDR and PR emphasizes the critical role of topology in dynamic performance. MDR favors modal sparsity and spectral compactness, whereas PR enhances stability under variations in internal forces. In both cases, simpler and symmetric topologies (A and B) achieve superior frequency robustness, while more complex architectures (C and D) trade controllability for richer, more sensitive dynamic behavior, illustrating the interplay between structural complexity, vibrational performance, and optimization objectives.

Figure 14 presents the frequency response of tensegrity structures optimized under the Critical FRF Magnitude (CFM) criterion. Under CFM optimization, simpler configurations (Topologies A and B) exhibit the lowest spectral amplitudes across the frequency range. Topology A achieves the most compact and stable response, indicating effective suppression of resonant amplification and highly damped dynamic behavior. Topology B follows a similar trend, with slightly higher amplitudes, reflecting modest sensitivity at mid-to-high frequencies.

In contrast, complex lattices (Topologies C and D) display larger spectral magnitudes and more pronounced fluctuations, particularly above 100 Hz. The sharper peaks highlight stronger modal interactions and less effective resonance suppression, arising from higher connectivity and additional degrees of freedom, which introduce localized flexibility and extra modal coupling paths. Overall, CFM optimization produces tensegrity structures with smoother and more controlled frequency responses. While simpler and symmetric topologies (A and B) achieve superior vibrational robustness, more intricate architectures (C and D) exhibit amplified sensitivity, reflecting the trade-off between geometric complexity and dynamic stability.

Across all analyzed optimization criteria, the frequency response results reveal consistent patterns linking dynamic performance, optimization objective, and topological complexity. Simpler and symmetric topologies (A and B) consistently achieve compact, stable spectra with minimal resonant amplification, indicating robust dynamic behavior regardless of the optimization metric. More complex and highly connected lattices (C and D), however, exhibit amplified responses, pronounced peaks, and irregular fluctuations, reflecting greater sensitivity to modal coupling, prestress variations, and high-frequency excitations. DE and PR generally favor static robustness and prestress stability, MMS and MDR enhance modal separation at the expense of higher spectral growth in dense topologies, and CFM explicitly minimizes peak amplitudes to improve vibrational resilience. Together, these observations highlight the inherent trade-offs in tensegrity design: dynamic robustness is maximized in simpler configurations, while complex topologies provide richer but less predictable spectral behavior, emphasizing the need to carefully select optimization metrics according to the intended functional priorities.

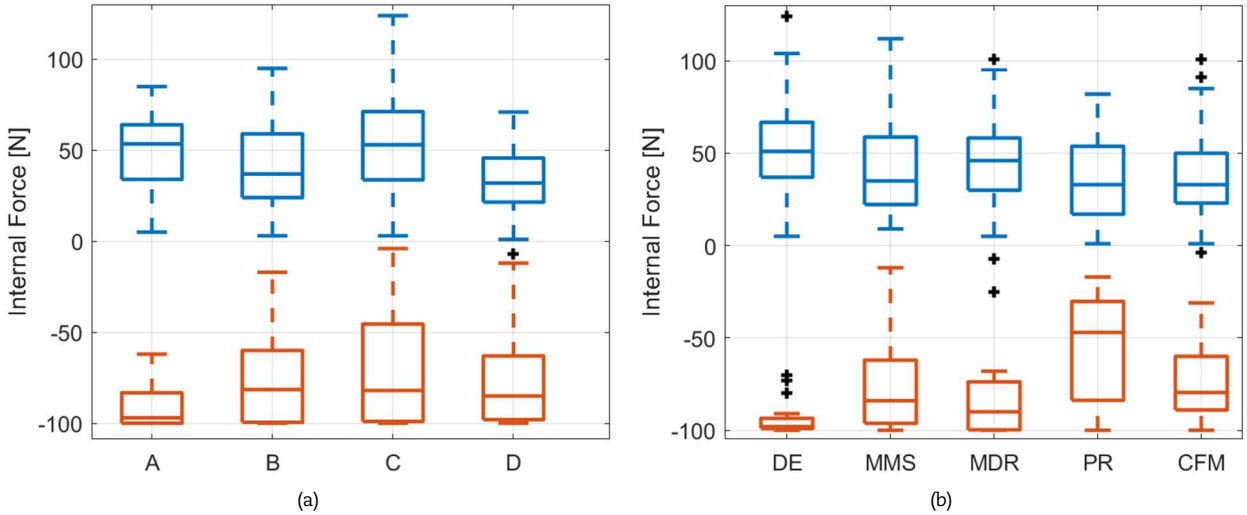

Fig. 15. Internal force distribution in optimized tensegrity structures, (a) by topology, (b) by metric.

Figure 15 illustrates the distribution of internal forces in the optimized tensegrity structures. Figure 15(a) shows the internal force distributions for the four topologies (A–D), separated into tensile (blue) and compressive (orange) elements. Topology A exhibits the most balanced behavior, with moderate force ranges and limited dispersion in both tension and compression, indicating efficient load transfer and uniform stress sharing among bars and cables. Topology B, in contrast, presents a wider spread in tensile forces, suggesting that some cables carry higher pre-tension, which may locally enhance stiffness but also increase stress concentration in certain members. Topologies C and D display trends associated with higher geometric complexity: in Topology C, several compressive elements have low or near-zero forces, reflecting partial load deactivation and uneven stress distribution, whereas Topology D achieves a more homogeneous tensile distribution and well-balanced compression forces, highlighting the benefits of higher connectivity and symmetry in mitigating local instabilities. Overall, these results underscore the strong influence of topology on internal stress balance and the efficiency of prestress transfer mechanisms.

Figure 15(b) presents the internal force distributions across structures optimized with five vibration-based metrics. The DE-optimized structures exhibit the most uniform compressive forces, indicating that prioritizing dynamic stiffness promotes an even load distribution. Some tensile members, however, experience higher forces, reflecting localized prestress increases driven by modal optimization. In contrast, MMS and PR optimizations produce more heterogeneous distributions, with compressive elements showing greater variability and partial deactivation in some bars, while tensile forces remain relatively balanced. MDR and CFM optimizations show similar tendencies, with higher variability in tensile forces and occasional predominance over compression, suggesting that these metrics encourage configurations that redistribute internal loads unevenly to enhance dynamic performance. Collectively, these observations highlight the trade-offs between internal stress uniformity and vibrational robustness: DE favors stiffness balance, while other metrics (MMS, MDR, PR, CFM) yield broader force spectra to achieve improved dynamic characteristics.

The internal force distributions in Fig. 15 are consistent with the material properties in Table 4. Tensile forces remain well below the cable strength, and compressive forces in the struts stay within the elastic range associated with their stiffness and slenderness. These magnitudes are typical of lightly prestressed tensegrity units and remain compatible with the linear elastic assumptions adopted throughout the spectral formulation. In addition, the stability condition $\Lambda > 0$ guarantees that all optimized configurations possess sufficient prestress to eliminate infinitesimal collapse modes, ensuring structural integrity independently of the exact force level.

Overall, the collective results reveal a coherent relationship between topology complexity, optimization metric, and dynamic performance of tensegrity structures. Simpler topologies (A and B) consistently achieve smoother convergence, more regular equilibrium configurations, and enhanced spectral compactness, indicating that geometric symmetry facilitates both stiffness and vibrational robustness. Conversely, complex systems (C and D) exhibit broader variability across metrics, leading to higher modal density, stronger prestress gradients, and larger spectral amplification under dynamic excitation. These effects underscore that topology and metric selection jointly define the attainable balance between stiffness uniformity, modal control, and prestress efficiency. Furthermore, the comparative analysis of internal forces demonstrates that optimization not only shapes global geometry but also redistributes local load paths, reinforcing the multiscale nature of tensegrity adaptation. Taken together, these findings provide a consistent foundation for the concluding interpretations presented in the next section, where the implications of these behaviors for tensegrity design and optimization are summarized.

6. Conclusion

This work presented a comprehensive framework for the optimization of tensegrity structures based exclusively on their vibrational performance, combining the Spectral Element Method (SEM) with Particle Swarm Optimization (PSO). The SEM formulation enabled high-fidelity simulations of the dynamic response of prestressed tensegrity cells, efficiently capturing natural frequencies, modal interactions, and frequency response functions (FRFs) without the computational burden associated with conventional finite element approaches. The PSO algorithm explored the design space across five vibration-oriented metrics—Dynamic Efficiency (DE), Minimum Modal Separation (MMS), Modal Density Ratio (MDR), Prestress Robustness (PR), and Critical FRF Magnitude (CFM)—allowing a multi-faceted assessment of dynamic behavior, stability, and structural robustness.

The optimization results highlight a clear distinction between objectives that are easier to optimize and those that are more challenging. Stiffness- and energy-related metrics such as DE and CFM consistently led to faster convergence, lower variability across repeated PSO runs, and optimized configurations with uniform compressive behavior and moderate tensile dispersion. Conversely, metrics like MMS and PR demonstrated slower convergence, higher sensitivity to nodal perturbations, and more heterogeneous internal force distributions, reflecting the influence of geometric nonlinearities, modal couplings, and prestress redistribution. The comparative analysis across topologies showed that simpler structures (Topologies A and B) reach stable optima

more rapidly, producing compact and predictable frequency responses, whereas more complex topologies (C and D) exhibit greater variability, delayed convergence, and highly specialized equilibrium configurations.

Analysis of the optimized configurations revealed systematic trade-offs between geometric regularity, modal separation, and robustness to prestress variation. DE- and CFM-driven solutions promoted globally balanced geometries, facilitating homogeneous stress distributions and stable vibrational behavior. In contrast, MMS, MDR, and PR optimization tended to generate asymmetrical or irregular configurations, enhancing specific modal properties or robustness at the expense of geometric uniformity. These observations underscore the critical role of the chosen performance metric in guiding the structural evolution of tensegrity cells and highlight the intricate interplay between topology, prestress distribution, and dynamic response.

From a practical perspective, the study demonstrates that PSO is an effective tool for exploring tensegrity design spaces, particularly for low- to moderate-dimensional systems. However, as topological complexity increases, optimization becomes more sensitive, runtime increases, and the likelihood that improving one metric adversely affects another grows. The frequency response and internal force analyses suggest that designers must carefully consider the target metric and the structural objectives, balancing stiffness, dynamic efficiency, and robustness according to application-specific priorities.

For future work, several directions can enhance the utility of the proposed framework. First, incorporating multi-objective or hybrid optimization strategies would allow simultaneous consideration of competing criteria, explicitly capturing trade-offs between stiffness, modal performance, and robustness. Second, extending the methodology to periodic tensegrity lattices using Bloch analysis could enable the design of bandgap structures or metamaterials, linking local prestress distributions to global wave propagation properties. Finally, integrating experimental validation, surrogate modeling, or adaptive optimization techniques would improve the convergence stability for highly nonlinear metrics and provide actionable insights for practical tensegrity designs. Overall, the present framework establishes a solid foundation for the vibration-oriented design of tensegrity structures, offering a systematic approach to achieving tailored dynamic performance, balanced internal forces, and controlled structural robustness.

Author Contributions

J.C. Guacheta-Alba planned the project, developed the computational models, conducted the simulations, and analyzed the results; L.S. Constantin Raptopoulos and M.S. Dutra supervised the research, provided guidance on methodology, reviewed the modeling and results, and contributed to the manuscript revision. The manuscript was written through the contribution of all authors. All authors discussed the results, reviewed, and approved the final version of the manuscript.

Acknowledgments

To CNPq and FAPERJ for the post-graduate scholarship, and the Automation and Robotics Laboratory (LabRob) at COPPE for the structure provided. The authors are grateful to Fundação Carlos Chagas Filho de Amparo à Pesquisa do Estado do Rio de Janeiro (FAPERJ), through Programa de Excelência Acadêmica (PROEX), for the nancial support on Process Number 201.731/2025.

Conflict of Interest

The authors declared no potential conflicts of interest concerning the research, authorship, and publication of this article.

Funding

The authors received no financial support for the research, authorship, and publication of this article.

Data Availability Statements

The datasets and computational materials supporting the findings of this study are publicly available at the following repository: https://github.com/juankg18/JACM-2510-5544. Additional data are available from the corresponding author upon reasonable request.

Nomenclature

$w(x,t)$	Transverse displacement of a member [m]	$\sigma_{min}(S_s(\omega))$	Smallest singular value of $S_s(\omega)$ [N/m]
ρ	Linear mass density [kg/m]	ω_1	Fundamental natural frequency [rad/s]
A	Cross-sectional area of a member [m^2]	M	Total mass of the structure [kg]
N	Axial force in the member (tension positive) [N]	DE	Dynamic Efficiency [rad·s^{-1}·kg^{-1}]
$W(x)$	Harmonic amplitude of transverse displacement [m]	MMS	Minimum Modal Separation [rad/s]
k	Wavenumber [rad/m]	MDR	Modal Density Ratio [rad^{-1}]
q_e	Prestress coefficient of element (e)	PR	Prestress Robustness [rad/s]
E	Young's modulus [Pa]	CFM	Critical FRF Magnitude [m]
L_e	Length of element (e) [m]	x_i	Particle position in PSO [m]
$S^{(e)}(\omega)$	Elemental spectral stiffness matrix [N/m]	v_i	Particle velocity in PSO [m/s]
$H^{(e)}(\omega)$	Dynamic shape function matrix	w, c_1, c_2	PSO inertia and acceleration coefficients
$D^{(e)}(\omega)$	Material and geometric properties of element (e)	p_i	Best previous particle position [m]
$T^{(e)}$	Transformation matrix from local to global coordinates	g	Best global particle position [m]
$A^{(e)}$	Connectivity matrix of element (e)	Λ	Projected stiffness for stability check [N/m]
$S_s(\omega)$	Global spectral matrix of the structure [N/m]	M	Basis of null space of equilibrium matrix
u	Nodal displacement vector [m]	D	Internal stiffness matrix [N/m]

References

[1] Mei, R., Liu, R., Wang, Y., Xu, X., Adaptive Vibration-Driven Tensegrity in Unstructured Environments, *Journal of Bionic Engineering*, 22(5), 2025, 2354-2366.
[2] Guacheta-Alba, J.C., Valencia-Castaneda, A.J., Dutra, M.S., Mauledoux, M., Aviles, O.F., *Tensegrity Approaches for Flexible Robots: A Review, in: Synergetic Cooperation between Robots and Humans*, Springer Nature Switzerland, 2024, 52–62.
[3] Goyal, R., Skelton, R.E., Tensegrity system dynamics with rigid bars and massive strings, *Multibody System Dynamics*, 46(3), 2019, 203-228.

[4] Liu, Y., Wang, W., Liu, T., Wu, S., Tang, G., Geometric Stiffness and Model Improvement of Rigid Elements for Preloaded Modal Analysis, *Journal of Computational and Nonlinear Dynamics*, 19(11), 2024, 111001.
[5] Guacheta-Alba, J.C., Valencia-Castañeda, A.J., Max Suell, M., Aviles, O.F., Mauledoux, M., New Approaches and Recent Applications of Tensegrity Structures, *Journal of Engineering Science and Technology Review*, 16(5), 2023, 1-12.
[6] Luo, J., Xu, X., Wu, Z., Wu, S., A unified approach to dynamic analysis of tensegrity structures with arbitrary rigid bodies and rigid bars, *Multibody System Dynamics*, 64(2), 2024, 245-276.
[7] Wang, Y., Xu, X., Luo, Y., Stability Conditions for General Tensegrity with Rigid Bodies, *Journal of Engineering Mechanics*, 149(8), 2023.
[8] Yuan, K., Yuan, S., Zhu, W., Full-Field Modal Analysis of a Tensegrity Column Using a Three-Dimensional Scanning Laser Doppler Vibrometer with a Mirror, *Journal of Vibration and Acoustics*, 146(6), 2024, 061101.
[9] Yaowen, O., Xiaodong, F., Miah, M.S., Active vibration control of tensegrity structures for performance enhancement: A comparative study, *Earthquake Engineering and Engineering Vibration*, 18(3), 2019, 679-693.
[10] Fan, L., Sun, Y., Fan, W., Chen, Y., Feng, J., Determination of active members and zero-stress states for symmetric prestressed cable–strut structures, *Acta Mechanica*, 231(9), 2020, 3607-3620.
[11] Gan, B.S., *Computational Modeling of Tensegrity Structures: Art, Nature, Mechanical and Biological Systems*, Springer International Publishing, 2020.
[12] Ma, S., Chen, M., Skelton, R.E., TsgFEM: Tensegrity Finite Element Method, *Journal of Open Source Software*, 7(75), 2022, 3390.
[13] Gan, B.S., *Self-vibrational Analysis of a Tensegrity, in: Modern Mechanics and Applications*, Springer Singapore, 2021, 87-99.
[14] Peng, H., Wang, M., Yang, H., Li, F., Kan, Z., Rigid-flexible-soft coupling dynamic modeling and analysis of clustered tensegrity, *Nonlinear Dynamics*, 112(13), 2024, 10959-10993.
[15] Lv, Q., Tang, Y., Wang, X., Li, T., A force-density framework for flexible multi-body dynamic analysis of clustered tensegrity structures, *International Journal of Solids and Structures*, 305, 2024, 113098.
[16] Liu, M., Cao, D., Wei, J., Survey on Equivalent Continuum Modeling for Truss Structures and Their Nonlinear Dynamics and Vibration Control, *Journal of Vibration Engineering & Technologies*, 10(2), 2021, 667-687.
[17] Akhtar, S., Sunny, M.R., Rest length controlled tunable band structure in periodic tensegrity metastructure – a numerical study using a novel consistent stiffness and mass formulation, *Mechanics of Advanced Materials and Structures*, 32(10), 2024, 2125-2139.
[18] Gan, B.S., Kiryu, S., Vibration of Tensegrity Structure by using SEM, *Journal of Advanced Civil and Environmental Engineering*, 2(2), 2019, 53-58.
[19] Gan, B.S., *Tensegrity for Mechanical Application: Vibration, in: Computational Modeling of Tensegrity Structures*, Springer International Publishing, 2019, 171-191.
[20] Nouchi, E., Oka, T., Kataoka, N., Kawano, Y., Gan, B.S., Study on Vibrational Behavior of Cytoskeletons Modeled by Cylindrical Tensegrity Structure, *bioRxiv*, 2023, 2023-06.
[21] Habibi, T., Rhode-Barbarigos, L., Keller, T., Effects of prestress implementation on self-stress state in large-scale tensegrity structure, *Engineering Structures*, 288, 2023, 116222.
[22] Wang, Y., Xu, X., Luo, Y., Topology Optimization of Tensegrity and Prestressed Cable-Strut Structures Considering Geometric Stiffness, *Journal of Structural Engineering*, 151(6), 2025, 104052.
[23] Vangelatos, Z., Micheletti, A., Grigoropoulos, C.P., Fraternali, F., Design and Testing of Bistable Lattices with Tensegrity Architecture and Nanoscale Features Fabricated by Multiphoton Lithography, *Nanomaterials*, 10(4), 2020, 652.
[24] Upadhyay, S.D., Singh, P.P., Thakur, V., Ranganathan, R., Recent advances in modeling structure–property relations in biomimetic materials at the molecular and continuum scales, *Journal of the American Ceramic Society*, 109(1), 2026, e70241.
[25] Oudich, M., Gerard, N.J.R., Deng, Y., Jing, Y., Tailoring Structure-Borne Sound through Bandgap Engineering in Phononic Crystals and Metamaterials: A Comprehensive Review, *Advanced Functional Materials*, 33(2), 2023, 2206309.
[26] Fiorini, G.A., Sánchez, J.A.G., Ramírez, C.Q., Paccola, R.R., Analysis of band structures using ω(k)- and k(ω)-approaches for two-dimensional truss metamaterials under residual strain and variations in mass distribution, *Mechanics of Advanced Materials and Structures*, 2025, 1-18.
[27] Jankowski, R., Manguri, A., Hassan, H., Saeed, N., Topology, Size, and Shape Optimization in Civil Engineering Structures: A Review, *Computer Modeling in Engineering & Sciences*, 142(2), 2025, 933–971.
[28] Feron, J., Boucher, L., Denoël, V., Latteur, P., Optimization of Footbridges Composed of Prismatic Tensegrity Modules, *Journal of Bridge Engineering*, 24(12), 2019, 04019112.
[29] Xiong, H., Zhou, T., Zhang, P., Shang, Z., Biswas, M., Li, H., Zhu, H., Optimization of Actuator Arrangement of Cable–Strut Tension Structures Based on Multi-Population Genetic Algorithm, *Symmetry*, 17(5), 2025, 695.
[30] Feng, X., Fan, Y., Peng, H., Chen, Y., Zheng, Y., Optimal Active Vibration Control of Tensegrity Structures Using Fast Model Predictive Control Strategy, *Structural Control and Health Monitoring*, 2023, 1–21.
[31] Rostami, P., Marzbanrad, J., Taghavi Parsa, M.H., Eigenfrequency-Based Topology Optimization Using Cooperative Coevolutionary Strategies and Moving Morphable Components, *Journal of the Brazilian Society of Mechanical Sciences and Engineering*, 44(5), 2022, 194.
[32] Hongyue, Z., Chuang, S., Hongwei, G., Rongqiang, L., Equivalent Mechanical Modeling and Dynamic Analysis of a Large Annular Tensegrity Structure, *Acta Mechanica*, 234(8), 2023, 3623–3647.
[33] Samaniego, E., Anitescu, C., Goswami, S., Nguyen-Thanh, V.M., Guo, H., Hamdia, K., Zhuang, X., Rabczuk, T., An energy approach to the solution of partial differential equations in computational mechanics via machine learning: Concepts, implementation and applications, *Computer Methods in Applied Mechanics and Engineering*, 362, 2020, 112790.
[34] Eshaghi, M.S., Anitescu, C., Thombre, M., Wang, Y., Zhuang, X., Rabczuk, T., Variational Physics-informed Neural Operator (VINO) for solving partial differential equations, *Computer Methods in Applied Mechanics and Engineering*, 437, 2025, 117785.
[33] Farajollahi, A., Seyyed Fakhrabadi, M.M., Prediction and Inverse Design of Bandgaps in Acoustic Metamaterials Using Deep Learning and Metaheuristic Optimization Techniques, *The European Physical Journal Plus*, 140(3), 2025, 213.
[34] Feng, X., Wang, X., Zhao, S., Lv, H., Zheng, Y., Vibration Control and Robustness Analysis of Tensegrity Structures via Fuzzy Dynamic Sliding Mode Control Method, *Structures*, 67, 2024, 106931.
[35] Song, N., Wang, M., Wang, X., Peng, H., A Novel Machine Learning Method for Real-Time Dynamic Analysis of Tensegrity Flexible Multibody Systems, *Nonlinear Dynamics*, 113(15), 2025, 19047–19074.
[36] Acar, O., Honkavaara, E., Botez, R.M., Bayburt, D.Ç., Mechanisms and Control Strategies for Morphing Structures in Quadrotors: A Review and Future Prospects, *Drones*, 9(9), 2025, 663.

ORCID iD

Juan C. Guacheta-Alba https://orcid.org/0000-0001-9949-9005
Luciano Santos Constantin Raptopoulos https://orcid.org/0000-0002-1774-3447
Max Suell Dutra https://orcid.org/0000-0003-3628-4749

© 2026 Shahid Chamran University of Ahvaz, Ahvaz, Iran. This article is an open access article distributed under the terms and conditions of the Creative Commons Attribution-NonCommercial 4.0 International (CC BY-NC 4.0 license) (http://creativecommons.org/licenses/by-nc/4.0/).

How to cite this article: Guacheta-Alba J.C., Raptopoulos L.S.C., Dutra M.S. Comparative Optimization of Vibrational Properties in Tensegrity Structures via Spectral Element Method, *J. Appl. Comput. Mech.*, 12(4), 2026, 1490-1506. https://doi.org/10.22055/jacm.2025.48846.5544

Publisher's Note Shahid Chamran University of Ahvaz remains neutral with regard to jurisdictional claims in published maps and institutional affiliations.